Inorganic Chemistry

Article

High-Pressure Behavior of Nickel Sulfate Monohydrate: Isothermal Compressibility, Structural Polymorphism, and Transition Pathway

Martin Ende,* Terhi Kirkkala, Michael Loitzenbauer, Dominik Talla, Manfred Wildner, and Ronald Miletich

Read Online

ACCESS | Metrics & More | Article Recommendations | Supporting Information

ABSTRACT: Single crystals of synthetic nickel sulfate monohydrate, α-NiSO$_4$·H$_2$O (space-group symmetry $C2/c$ at ambient conditions), were subject to high-pressure behavior investigations in a diamond-anvil cell up to 10.8 GPa. By means of subtle spectral changes in Raman spectra recorded at 298 K on isothermal compression, two discontinuities were identified at 2.47(1) and 6.5(5) GPa. Both transitions turn out to be apparently second order in character, as deduced from the continuous evolution of unit-cell volumes determined from single-crystal X-ray diffraction. The first structural transition from α- to β-NiSO$_4$·H$_2$O is an obvious ferroelastic $C2/c$–$P\bar{1}$ transition. It is purely displacive from a structural point of view, accompanied by symmetry changes in the hydrogen-bonding scheme. The second β- to γ-NiSO$_4$·H$_2$O transition, further splitting the O2 (hydrogen bridge acceptor) position and violating the $P\bar{1}$ space-group symmetry, is also evident from the splitting of individual bands in the Raman spectra. It can be attributed to symmetry reduction through local violation of local centrosymmetry. Lattice elasticities were obtained by fitting second-order Birch−Murnaghan equations of state to the p-V data points yielding the following zero-pressure bulk moduli values: K_0 = 63.4 ± 1.0 GPa for α-NiSO$_4$·H$_2$O, K_0 = 61.3 ± 1.9 GPa for β-NiSO$_4$·H$_2$O, and K_0 = 68.8 ± 2.5 GPa for γ-NiSO$_4$·H$_2$O.
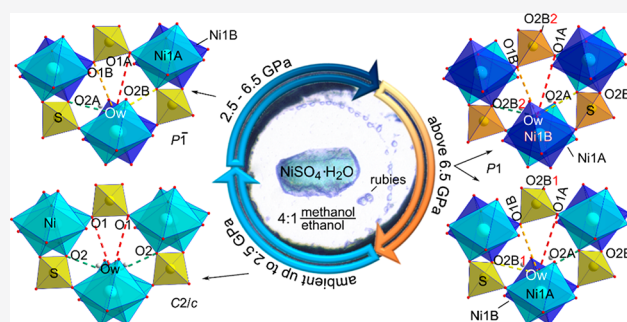
INTRODUCTION

Hydrated sulfate salts and their behavior under extreme conditions are the subject of intensive research, as they are widespread on surfaces of planets, their moons, and presumably even exoplanets.[1−6] The extreme temperature (T) oscillations on planetary surfaces and the extraordinary pressures (p), along with high-p/high-T variations inside the icy satellites, may lead to structural instabilities and phase transitions. This may include changes of the hydration state, as exemplified by the p-induced dehydration reactions and described for the MgSO$_4$·nH$_2$O (0 ≤ n ≤ 11) series.[7−10] However, it can also involve incongruent melting[11] or polymorphism with associated structural phase transitions.[12] The Ni-enrichment in solid phases[5] in the ternary system NiSO$_4$−MgSO$_4$−H$_2$O together with high Ni concentrations in the sulfate-rich soluble fraction of natural meteorite samples[13] emphasize the particular importance of nickel sulfate components, which are also known as the rare terrestrial hydrate minerals morenosite (n = 7), retgersite (n = 6), and dwornikite (n = 1).[14]

The monohydrates of divalent cations have received particular attention, since they apparently represent considerably stable solids. They have been observed on Mars and Jovian moons Ganymede and Callisto, preferably as the monohydrated magnesium sulfate mineral kieserite. Their large structural flexibility leads to the existence of various end-member representatives (M^{2+}SO$_4$·H$_2$O with M^{2+}= Mg, Mn, Fe, Co, Ni, Zn)[15,16] and their solid solutions.[17−19] This also includes selenates,[20] and in rare cases even phosphates such as Mn^{3+}PO$_4$·H$_2$O.[21,22] The structure type has already been determined in space group $C2/c$ by Leonhard and Weiss.[23] It can be described as a three-dimensional heterodesmic framework, which consists of continuous octahedral chains of corner-sharing [MO$_4$(H$_2$O)$_2$]$^{6-}$ units running along the [001] direction, and which are cross-linked through the tetrahedral SO$_4$ units. Within the given $C2/c$ symmetry, the M and S atoms each occupy a single crystallographic site. The barycenter of the water molecule (Ow) is also located on a unique site. Due to the site symmetry of the Ow atoms on this position, the hydrogen bonding system exhibits 2-fold symmetry with two Ow-H⋯O hydrogen bonds of medium strength,[15,24,25] as well as two further intermolecular O⋯O
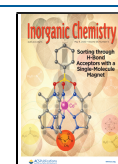
contacts, not involved in the H-bonding scheme under ambient conditions.

Apart from the kieserite aristotype compounds with $C2/c$ symmetry, $CdSO_4 \cdot H_2O$ was found to crystallize in a different monoclinic space-group symmetry,[26] i.e., in the maximal nonisomorphic subgroup $P2_1/n$, which was attributed to the relatively larger size of the Cd^{2+} atoms located on the octahedral site. Moreover, the Jahn–Teller effect of Cu^{2+} was found to be responsible for a cooperative lattice distortion resulting in the triclinic space group $P\bar{1}$ in $CuSO_4 \cdot H_2O$.[16,25] Recent investigations on $MgSO_4 \cdot H_2O$ and $FeSO_4 \cdot H_2O$ under hydrostatic compression revealed a ferroelastic phase transition following the *translationsgleiche* $C2/c$-$P\bar{1}$ group–subgroup relation and being apparently second order in its thermodynamic character.[27,28] Any of the symmetry changes follow a pattern of atom displacements related to the changes within the hydrogen bonding systems, whereas the topology of the heterodesmic frameworks remains unchanged, apart from distortion originating from symmetry breaking. In this context, synthetic $NiSO_4 \cdot H_2O$ single crystals are investigated in this study with respect to the occurrence of an equivalent structural polymorphism. In particular, we examine how the critical size and the electronic configuration of the cations on the M site influence the stability of the low-symmetry polymorphs to better understand the mechanism and pathway of structural transitions. Investigation of the high-p behavior of the Ni end member of this type of sulfate is essential from the cosmochemical point of view, given the potential presence and distribution of hydrated sulfates inside icy planetary bodies.

MATERIALS AND METHODS

Synthesis. Sample crystals were grown under low hydrothermal conditions using a similar technique to that described by Talla and Wildner[29] within a temperature range between room temperature and 210 °C at moderate autogenous vapor pressures using polytetrafluoroethylene (PTFE)-lined autoclaves. Subeuhedral crystals formed from a supersaturated aqueous solution of sulfuric acid (~0.25–0.75 mL concentrated H_2SO_4 (98%) + ~0.5 mL H_2O) added to ~0.3 g of $NiSO_4 \cdot 7H_2O$ (Alfa Aesar, p.a.) inside the PTFE reaction chambers with ~3–4 cm^3 volume capacity. It was kept at $T = 220$ °C for 14 days and then cooled down to RT. The solid products were finally washed with pure H_2O and ethanol and then dried overnight at $T = 75$ °C (cf. Supporting Information for more data).

High-Pressure Sample Environment. Selected crystals were loaded into *ETH-type*[30] diamond-anvil cells (DAC) equipped with either standard brilliant-cut or Böhler Almax-type[31] type-I diamond anvils with culet faces of ∅ = 600 μm. Pressure chambers with ∅ ≈ 250 μm were prepared using stainless steel gaskets preindented to ~90–100 μm thickness. A 4:1 methanol–ethanol mixture was used as a p-transmitting medium for the single-crystal X-ray diffraction (scXRD) investigations, while in situ vibrational spectroscopy was carried out on crystals pressurized in cryogenically loaded argon. Pressures were determined using conventional quartz and ruby standards, following the calibration of Scheidl et al.[32] and Jacobsen et al.,[33] respectively. The estimated standard deviations (ESDs) of the p values obtained by the internal quartz standard were determined from the ESDs of the measured p-dependent unit-cell volume (V). The ESDs of the p obtained from the R_1-line shift of the ruby luminescence spectra were estimated to be ±0.06 GPa after averaging repeated measurements.

Raman Spectroscopy. In-situ high-p Raman spectroscopy was carried out on several crystals (40 × 60 × 15 μm^3, 110 × 95 × 20 μm^3, 80 × 80 × 40 μm^3, 40 × 50 × 40 μm^3), together with ruby spheres as pressure calibrants,[34,35] all compressed in dense liquefied Ar. Spectra were collected by means of a confocal Horiba Jobin Yvon

LabRAM-HR 800 spectrometer using a red He–Nd laser source emitting a beam with a wavelength of 632.8 nm and 20 mW, an Olympus BX41 microscope, and a mercury–cadmium–telluride detector. An Olympus LMPlanFL N 50× objective with a long working distance of 10.6 mm enabled focus of the laser beam onto the sample crystal inside the p chamber. A diffraction grating with 600 lines per millimeter was used for the measurements. High-p spectra were acquired using the software *LabSpec 6* (HORIBA Scientific) in the spectral range from the 35 to 1190 cm^{-1} shift with an exposure time of 60 s and two accumulations. The recorded spectra were fitted with the Gauss-Lorentz-area method after background subtraction achieved using the program *Peakfit 4.1.2* (*Systat Software Inc.*).

Precise Measurement of Lattice Parameters. Sample crystals were compressed in a conventional methanol–ethanol mixture together with a quartz single crystal serving as the p reference. XRD Bragg peak positions were measured on a *Stoe AED II* and *Huber 5042* diffractometer using a conventional scintillation counter and non-monochromatized Mo radiation, with the peak centering procedure being controlled through the *SINGLE*[36] software. For each hydrostatic p point, 16 to 23 individual Bragg reflections were measured in the 8-position centering mode[37] to refine the respective unit-cell volumes. Lattice parameters were refined in a first step without any symmetry constraints in order to identify possible deviations in metrics and were finally constrained to monoclinic symmetry, if applicable. The equations of state (EoS) were fitted by applying weighted least-squares techniques using the software *EoSFit7*.[38] Normalized pressure-strain analyses were carried out in order to determine the relevant order of truncation of the Birch–Murnaghan (BM) EoS.

High-Pressure Crystallography. The scXRD intensity data collections were performed on a sample crystal (~140 × 70 × 40 μm^3) loaded in a methanol–ethanol mixture (see Supporting Information, Figure S1). The data sets were measured on a Stoe StadiVari X-ray diffractometer using a DECTRIS Pilatus 300 K detector with a 450 μm silicon layer and an air-cooled Incoatec IμS molybdenum high-brilliance microfocus tube source (50 kV, 1 mA, beam size ≈ 110 μm) at $p = 0.6(1)$, $2.3(1)$, $4.5(1)$, and $8.4(1)$ GPa. Frames were collected with angular steps of 0.5° in ω rotational mode with the χ circle fixed to a value ranging from 0° to 90°. Data were collected on both sides of the DAC as achieved by a 180° rotation of the φ circle after each run. The exposure time was set to 100 s per frame. Intensities were integrated using the X-area 1.72 (STOE& Cie GmbH) software and corrected for absorption through the sample and DAC components by using the *ABSORB*[39] code. Indexing of the reconstructed reciprocal space yielded monoclinic lattice metrics for the measurements at $0.6(1)$ and $2.3(1)$ GPa, while at $4.5(1)$ and $8.4(1)$ GPa triclinic metrics were found. Initial positional parameters for the refinements were assigned according to those reported by Meusburger et al.[28] All refinements were carried out using scattering curves from the International Tables for Crystallography[40] and isotropic displacement parameters for all atoms using *SHELXL*[41] and the graphical user interface *ShelXle*.[42]

RESULTS AND DISCUSSION

Evidence for Transformations in Raman Spectra. A sequence of, in total, 17 Raman spectra of $NiSO_4 \cdot H_2O$, as recorded in situ under hydrostatic high-p conditions between $0.46(6)$ and $10.80(6)$ GPa, is displayed in the Figures 1 and 2 for the Raman shift range 35–1190 cm^{-1}. Any attempt to measure the vibrational response related to the H_2O molecule for the Raman shift range 2600–3500 cm^{-1} failed because of luminescence contributions from the sample and the diamond anvils. A focus on the internal modes in the ranges 35–690 cm^{-1} (Figure 1) and 970–1190 cm^{-1} (Figure 2) revealed the most prominent bands as described for isostructural $MgSO_4 \cdot H_2O$ and $FeSO_4 \cdot H_2O$.[27–29,43] These are the external lattice vibrational modes with wavenumbers (as determined at 1 bar) assigned to 129 and 138 cm^{-1} (lattice vibrations); 200, 246,
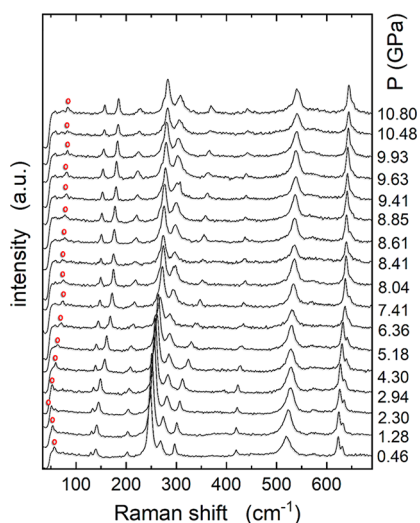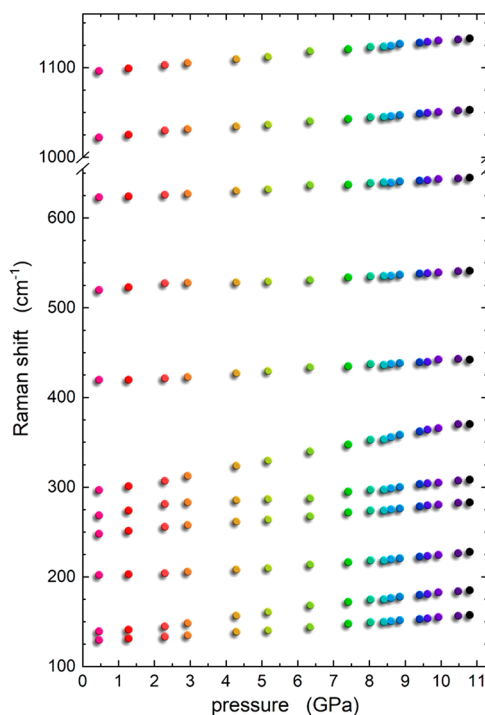
Figure 1. Sequence of high-pressure Raman spectra obtained from a $NiSO_4 \cdot H_2O$ single crystal under hydrostatic compression, indicating a phase transition occurring between 2.30(6) and 2.94(6) GPa.
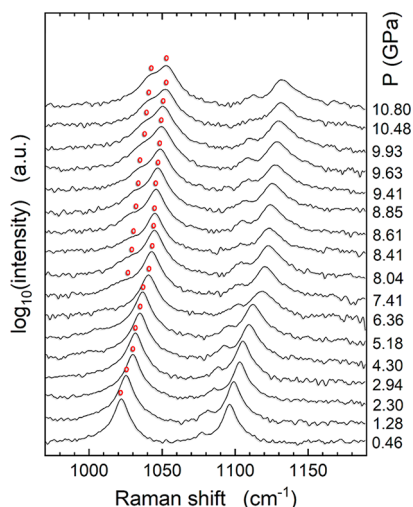
Figure 2. A close-up of the sulfate stretching bands of $NiSO_4 \cdot H_2O$. The emerging shoulder on the low-energy side of the marked Raman band, evident in all Raman spectra at $p > 6.4$ GPa, indicates the second phase transition with a critical transition point between 6.36(6) and 7.41(6) GPa.

Figure 3. Pressure dependence $\Delta\bar{\nu}/\Delta p$ of selected Raman bands as obtained from in situ high-pressure Raman spectra of $NiSO_4 \cdot H_2O$. Specific data point colors help to interpret the correlation matrix and PCA plot (Figure S3).

265, and 295 cm^{-1} (translational modes of either the octahedrally coordinated M position or the H_2O ligand); 419 and 518 cm^{-1} (ν_2 mode of SO_4); 622 and 629 cm^{-1} (ν_4 of SO_4); 1021 cm^{-1} (ν_1 of SO_4); and 1040, 1076, and 1095 cm^{-1} (ν_3 of SO_4). For a further detailed description, see Talla et al.[44] The high-p spectra reveal the typical average blueshifts with $\Delta\bar{\nu}/\Delta p$ values ranging between 2.42(7) and 7.45(8) cm^{-1} GPa^{-1} (Figure 3).

The spectral evolution and the lack of drastic changes with respect to band positions, numbers, and intensities of modes suggest that the structural topology should be largely retained across the recorded p range. Nevertheless, subtle and more or less pronounced changes in the $\Delta\bar{\nu}/\Delta p$ rates can be observed, which suggests two intervals of potential structural changes, i.e., between 2.30(6) and 2.94(6) GPa (Figure 1) and between 6.36(6) and 7.41(6) GPa (Figure 2). Apart from an emerging shoulder followed by a significant splitting of the $\nu_1(SO_4)$
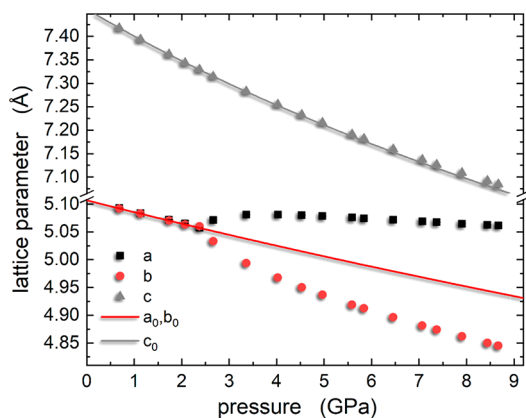
mode located at 1021 cm^{-1} (at 1 bar), new weak modes in the low-frequency range similar to those reported for $MgSO_4 \cdot H_2O$ and $FeSO_4 \cdot H_2O$[27,28] have not been observed. This can be simply explained as the arbitrary orientation of samples does not necessarily allow all modes to be recognizable with comparable intensities. Compared to Meusburger et al.,[27,28] in $NiSO_4 \cdot H_2O$ there is evidence for a second potential structural change within the experimentally accessible p regime. The first is represented by a potential soft mode, which is just within the measurable range around 58 cm^{-1} (at 1 bar, Figure 1). Taking a closer look at the splitting of the Raman band attributed to the $\nu_1(SO_4)$ mode indicates that there is more than one crystallographic independent sulfate group in the structure. The careful analysis of the spectra (Figure 2) shows that the second band component starts emerging at $p \geq 7.41(6)$ GPa, and thus these spectral changes coincide with the second supposed discontinuity as described above. Considering that for the earlier reported $C2/c$-$P\bar{1}$ transition in isostructural compounds[27,28] the structures of both polymorphs exhibit just one single S position, the second structural change must be accompanied by continued symmetry breaking, leading to the diversification of more than one S site. The current observation may thus be a possible indication of another structural change, which has not yet been recognized so far. In decompression, the second Raman band component seems to vanish at $p \leq 5.60(6)$ GPa (Figure S4), which means that the second potential transformation in contrast to the first one would show a hysteresis of about 1.8 GPa.

A detailed analysis of the fitted pressure-dependent Raman band shifts (Figure 3) in addition to a correlation matrix of these band positions especially in the region between 240 and 525 cm^{-1} (see the Supporting Information, Figure S3) support the observation of two distinct structural transitions in $NiSO_4 \cdot$

H_2O, especially with a subsequent principal component analysis (PCA) of these data (Figure S3, top right). This technique was for example previously successfully applied on Raman and powder X-ray diffraction data for the detection of subtle second order phase transitions in lawsonite.[45] However, only the second phase transition between 6.36(6) and 7.41(6) GPa could clearly be identified by a subsequent hierarchical cluster analysis (see dendrogram in the Supporting Information, Figure S2). The first two clusters, separated between 2.94(6) and 4.30(6) GPa, are most likely influenced by the relatively larger pressure steps facilitated under low pressure conditions. Tentative clusters were shown in the PCA plot (Figure S3, top right) using three ellipses. In some Raman band shift correlations, however, this separation is more obvious as manifested by a sudden discontinuity located between 2.30(6) and 2.94(6) GPa.
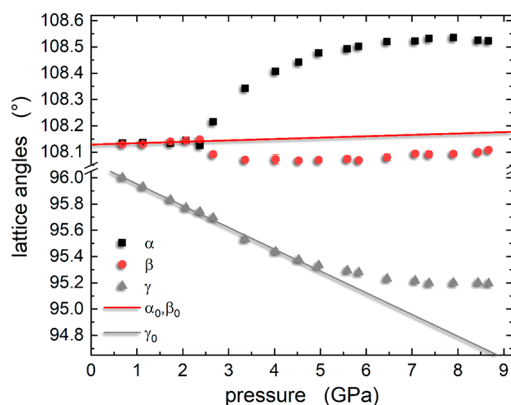
Lattice Properties under Isothermal Compression.
Precise unit-cell parameters and unit-cell volumes were determined at 18 individual pressure points within the pressure range 10^{-4} to 8.67(1) GPa by means of single-crystal diffraction and applying unconstrained refinements of metric parameters (see Table S1 in the Supporting Information). In order to facilitate the comparison between monoclinic and triclinic lattices, the lattice parameters are provided in addition to the standard monoclinic $C2/c$ setting in that of the reduced cell (with $a_{red} = b_{red} \neq c_{red}$, $\alpha_{red} = \beta_{red} \neq \gamma_{red}$ for a monoclinic metric, see Supporting Information, Table S2). Plotting the cell parameters (Figure 4) and lattice angles (Figure 5) as a

Figure 5. Pressure-dependent evolution of the unit-cell angles in the basis-vector setting of the reduced cell. The red and gray lines correspond to linear fits including the data points up to 2.5 GPa.

following the typical trend of nonlinear length change with pressure.

As the Raman spectra reveal several hints for the occurrence of a second subtle structural change, the evolution of the lattice parameters was carefully inspected with respect to changes in the p interval around the second critical pressure between 6.36(6) and 7.41(6) GPa. There is no conspicuous deviation or any significant discontinuity recognizable in the p dependencies of the base vectors. It requires a very careful inspection to recognize very subtle deviations as exemplified in Figure 6. This plot shows the differences of the c-axis values in

Figure 4. Pressure-dependent evolution of the unit-cell basis vectors a, b, and c. The red and gray lines correspond to fits of BM-2 EoS up to 2.5 GPa, with the respective parameters for the axial moduli as quoted in Table 1.
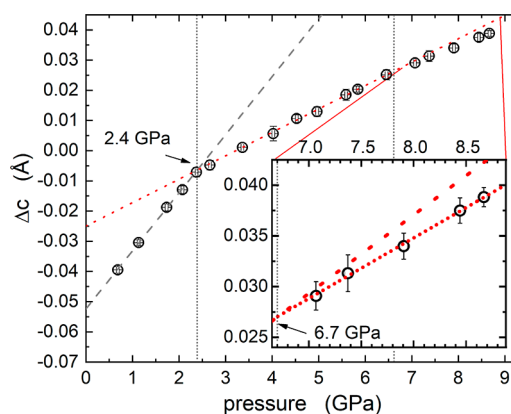

Figure 6. Pressure dependent evolution of Δc between the two possible reduced cell settings mutually related by the transformation matrix ($\bar{1}00/0\bar{1}0/111$). It clearly shows the first phase transformation in $NiSO_4 \cdot H_2O$ at 2.4 GPa and a possible second discontinuity (visible in enlarged section) starting around 6.7 GPa.

function of p, there is clear evidence of an obvious lattice distortion from monoclinic ($a_{red} = b_{red}$, $\alpha_{red} = \beta_{red}$) to triclinic symmetry ($a_{red} \neq b_{red}$, $\alpha_{red} \neq \beta_{red}$) at ~2.66(1) GPa. The character of lattice distortion is identical to what has been observed for the isostructural compounds of Mg[28] and Fe,[27] and hence it can be assumed that it is the equivalent $C2/c-P\bar{1}$ transformation. The evolution of all three lattice angles α, β, and γ with p (Figure 5) provides again a clear proof in α and β for this first discontinuity, which starts between 2.38(1) and 2.66(1) GPa. This is less obvious for the refined base vector c (Figure 4). While a and b reveal a clear disproportionation of their values in the setting of the reduced cell, the c axis appears to shrink continuously even across the first discontinuity

the two possible settings of the reduced cell, thus exhibiting a distinct change in the $\Delta c/\Delta p$ rate of the linear trends with both lines intersecting around 2.4 GPa. The second linear trend line, as fitted to the data in the p interval 2.7−6 GPa, matches perfectly the linear relationship for the data points above the first discontinuity up to a pressure around 6.7 GPa. At this point, the last four data points clearly deviate by following another third linear trend at a deliberately lower $\Delta c/\Delta p$ rate, thus falling slightly below the second trendline. The onset point for the second change (6.7 GPa) perfectly coincides with the pressure range between 6.36(6) and 7.41(6) GPa as determined from Raman spectroscopy, at which the splitting of the $\nu_1(SO_4)$ band has been observed.

A similar deviation can be observed for evaluating the spontaneous strain components e_1 and e_2, which can be expected to be proportional to the order parameter for a continuous second order phase transition from monoclinic to triclinic symmetry (Figure 7). The values of the spontaneous
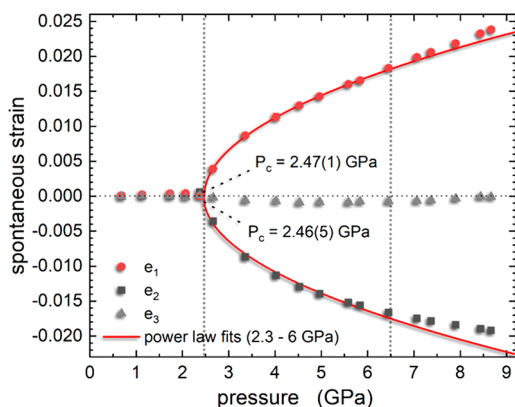
Figure 7. Components e_1, e_2, and e_3 of the spontaneous strain arising for the ferroelastic transition in $NiSO_4 \cdot H_2O$. Values are derived from Carpenter et al.[46] from extrapolated EoS fits provided in Figures 4 and 5 using the lattice parameters of the reduced cell. Red lines correspond to fitted power law functions with an ideal critical exponent $\beta = 0.5$. Vertical dotted lines represent the supposed transition pressures and reveal recognizable discrepancies for e_1 and e_2 components above 6.5 GPa.

strain components e_1, e_2, and e_3 were calculated from the lattice parameters of the triclinic reduced cell using the extrapolated fits shown in Figures 4 and 5 and derived from eqs 1−3) discussed in Carpenter et al.[46] for phase transitions between two triclinic forms (with β^* and β_0^* being the corresponding reciprocal lattice angles).

$$e_1 = e_{11} = a \sin(\gamma)/a_0 \sin(\gamma_0) - 1 \tag{1}$$

$$e_2 = e_{22} = b/b_0 - 1 \tag{2}$$

$$e_3 = e_{33} = c \sin(\alpha) \sin(\beta^*)/c_0 \sin(\alpha_0) \sin(\beta^*_0) - 1 \tag{3}$$

The plot in Figure 7 shows nonzero values starting at 2.66(1) GPa, which clearly follow a nonlinear $\Delta \propto |p - p_{crit}|^\beta$ trend. The critical exponent β was found to be very close to 1/2, such as found for both isostructural phases $MgSO_4 \cdot H_2O$ and $FeSO_4 \cdot H_2O$, thus suggesting the $C2/c - P\bar{1}$ being proper second order from the point of view of Landau theory.[27,28] The equivalent fits onto the spontaneous strain values with β constrained to 1/2 reveal clear deviations starting around 6.5 GPa. The values for the critical pressure p_c obtained from the fits (= 2.47 and 2.46 GPa) confirm the pressure of the monoclinic-to-triclinic transition with an uncertainty of 0.05− 0.01 GPa. The critical pressure for the second transition at 6.5 GPa can only be specified with a considerably greater inaccuracy of ±0.5 GPa.

Comparative Lattice Elasticities of Polymorphs. Changes of individual lattice parameters and the unit-cell
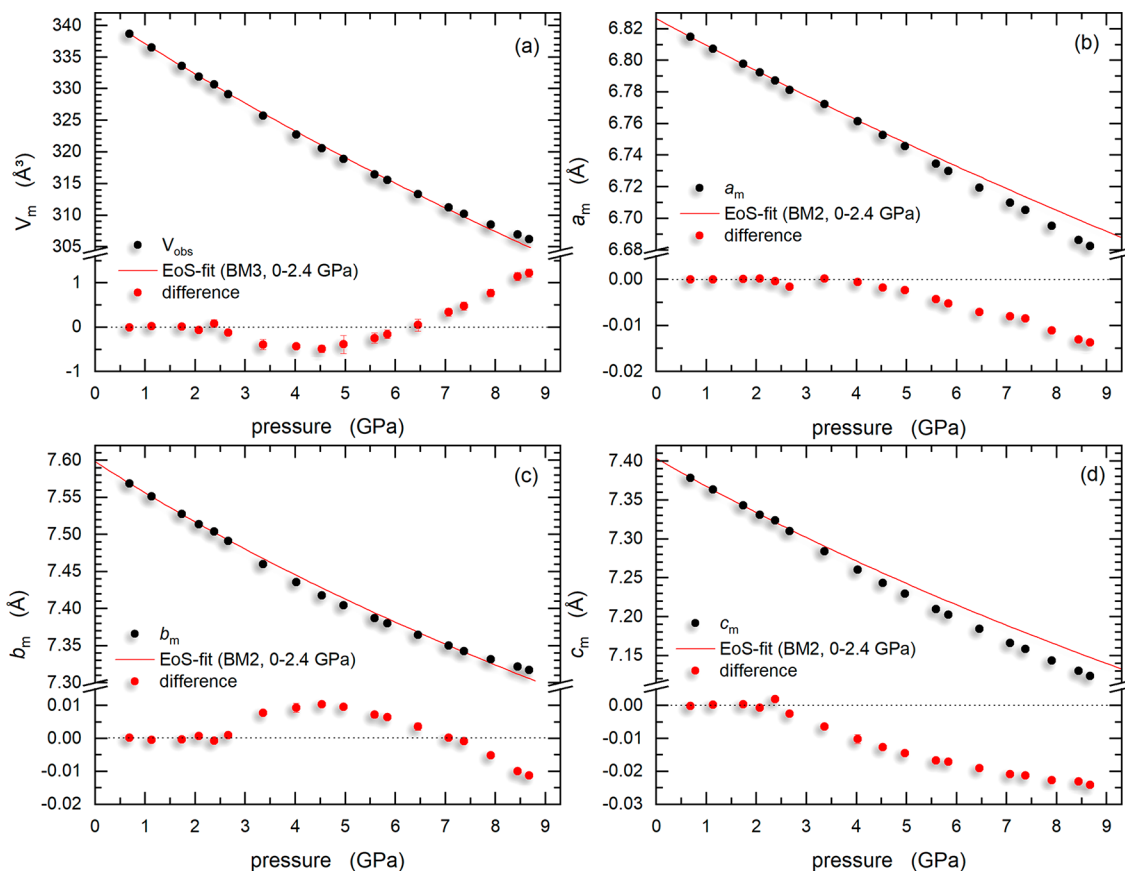
Figure 8. Evolution of the unit-cell parameters of $NiSO_4 \cdot H_2O$ in the $C2/c$ base-vector setting: (a) volume, (b) lattice parameter a, (c) lattice parameter b, and (d) lattice parameter c. Plots correspond to the data provided in Table S2. Red lines correspond to fits of BM-2 EoS with the respective parameters as quoted in the text.

Table 1. Least-Square Fitted BM-EoS Parameters of the Unit-Cell Volume and Lattice Parameters for Various End Member $MSO_4 \cdot H_2O$ Polymorphs

phase, p range (GPa)	X_0	K_0, M_0 (GPa)	K', M'	phase P range (GPa)	X_0	K_0, M_0 (GPa)	K', M'
α-$FeSO_4 \cdot H_2O$[a]	$V_0 = 365.2(3)$	$K_0 = 45.2(2)$	$K' = 6.7(1)$	α-$NiSO_4 \cdot H_2O$	$V_0 = 342.3(1)$	$K_0 = 63.4(1.0)$	$K' = 4$[b]
$10^{-4} - 5.94$	$a_0 = 7.082(1)$	$M_0 = 496(9)$	$M' = 1.3(3.2)$	$10^{-4} - 2.30$	$a_0 = 6.826(1)$	$M_0 = 401(12)$	$M' = 12$[b]
	$b_0 = 7.553(1)$	$M_0 = 109(2)$	$M' = 36(2)$		$b_0 = 7.598(1)$	$M_0 = 175(4)$	$M' = 12$[b]
	$c_0 = 7.779(1)$	$M_0 = 93.8(7)$	$M' = 13.1(4)$		$c_0 = 7.403(1)$	$M_0 = 200(4)$	$M' = 12$[b]
β-$FeSO_4 \cdot H_2O$[a]	$V_0 = 367.0(4)$	$K_0 = 45.1(6)$	$K' = 5.4$[c]	β-$NiSO_4 \cdot H_2O$	$V_0 = 342.1(6)$	$K_0 = 61.3(1.9)$	$K' = 4$[b]
$6.15 - 8.40$	$a_0 = 7.087(4)$	$M_0 = 471(19)$	$M' = 3.0$[c]	$4.00 - 6.00$	$a_0 = 6.838(4)$	$M_0 = 332(16)$	$M' = 12$[b]
	$b_0 = 7.54(1)$	$M_0 = 112(7)$	$M' = 36.8$[c]		$b_0 = 7.576(6)$	$M_0 = 191(7)$	$M' = 12$[b]
	$c_0 = 7.784(4)$	$M_0 = 102(1)$	$M' = 9.1$[c]		$c_0 = 7.414(6)$	$M_0 = 169(6)$	$M' = 12$[b]
α-$MgSO_4 \cdot H_2O$[a]	$V_0 = 355.5(4)$	$K_0 = 48.1(5)$	$K' = 8.1(6)$	γ-$NiSO_4 \cdot H_2O$	$V_0 = 339.5(8)$	$K_0 = 68.4(2.0)$	$K' = 4$[b]
$10^{-4} - 2.50$	$a_0 = 6.909(1)$	$M_0 = 297(12)$	$M' = 21(14)$	$6.50 - 9.00$	$a_0 = 6.850(6)$	$M_0 = 301(12)$	$M' = 12$[b]
	$b_0 = 7.628(1)$	$M_0 = 142(4)$	$M' = 30(5)$		$b_0 = 7.523(6)$	$M_0 = 264(9)$	$M' = 12$[b]
	$c_0 = 7.642(1)$	$M_0 = 94.1(1.3)$	$M' = 13.1(4)$		$c_0 = 7.405(7)$	$M_0 = 177(6)$	$M' = 12$[b]
β-$MgSO_4 \cdot H_2O$[a]	$V_0 = 355.8(1.8)$	$K_0 = 49.3(5.5)$	$K' = 4.8(1.0)$				
$4.75 - 8.40$	$a_0 = 6.911(1)$	$M_0 = 383(27)$	$M' = -6(2)$				
	$b_0 = 7.649(1)$	$M_0 = 83.5(5.5)$	$M' = 45.9(5.5)$				
	$c_0 = 7.615(14)$	$M_0 = 122(11)$	$M' = 8.0(1.5)$				

[a]Data for Mg and Fe polymorphs from Meusburger et al.[27,28] [b]Fixed value due to fit with BM-2 EoS. [c]c.f. Meusburger et al.[27]

Table 2. Parameters of the scXRD Data Collection and Results of the Structure Refinements of $NiSO_4 \cdot H_2O$

pressure (GPa)/$T = 298(1)$ K	0.6(1)	2.3(1)	4.5(1)	8.4(1)	8.4(1)
space group	$C2/c$ (15)	$C2/c$ (15)	$P\bar{1}$(2)	$P\bar{1}$(2)	$P\bar{1}$ (2) disordered
a (Å)	6.814(1)	6.786(1)	cf. a^*	cf. a^*	cf. a^*
b (Å)	7.569(1)	7.502(1)	cf. b^*	cf. b^*	cf. b^*
c (Å)	7.418(1)	7.329(1)	cf. c^*	cf. c^*	cf. c^*
a^a (Å)	5.093(1)	5.059(1)	4.950(1)	4.850(1)	4.850(1)
b^a (Å)	5.092(1)	5.060(1)	5.080(1)	5.063(1)	5.063(1)
c^a (Å)	7.418(1)	7.329(1)	7.233(1)	7.093(1)	7.093(1)
α (deg)	90	90	cf. α^*	cf. α^*	cf. α^*
β (deg)	117.72(1)	117.67(1)	cf. β^*	cf. β^*	cf. β^*
γ (deg)	90	90	cf. γ^*	cf. γ^*	cf. γ^*
α^a (deg)	108.14(1)	108.13(1)	108.07(1)	108.10(1)	108.10(1)
β^a (deg)	108.13(1)	108.14(1)	108.44(1)	108.53(1)	108.53(1)
γ^a (deg)	96.00(1)	95.74(1)	95.38(1)	95.20	95.20
V (Å^3)	338.7(1)	330.4(1)	160.3(1)	153.5(1)	153.5(1)
Z	4	4	2	2	2
no. runs/frames	20/1520	20/1520	20/1520	20/1520	20/1520
scan time (sec)	50	50	80	100	100
no. measured reflns	1550	1332	1359	1316	1316
no. unique reflns (obs/all)	184, 195	156, 159	277, 295	263, 282	263, 282
max. 2θ (deg)	73.10	72.66	72.06	72.96	72.96
R_{int}, R_{sigma} (%)	2.61, 1.12	2.41, 1.00	3.29, 1.73	3.29, 1.91	3.29, 1.91
R1(obs/all) (%)	3.25, 3.44	2.93, 2.97	2.85, 3.09	2.62, 2.81	2.46, 2.66
wR2 (%)	8.55	7.48	7.80	6.94	6.45
GoF	1.12	1.13	1.08	1.13	1.06
refined/constrained parameters	18/0	16/3	24/5	24/5	27/6
weight parameters, a and b[b]	0.059, 1.282	0.046, 1.894	0.050, 0.372	0.036, 0.423	0.047, 0.305
max/min electron density (e$^-$Å^{-3})	0.512, -0.479	0.463, -0.350	0.439, -0.358	0.363, -0.314	0.300, -0.282

[a]Lattice parameters of the reduced cell [b]$w = 1/\{\sigma 2(F_o^2) + [a \times P]2 + b \times P\}$; $P = ([\max(0, F_o^2)] + 2 \times F_c^2)/3$.

volume (V) follow the typical nonlinear trend lines on compression. On the basis of the small uncertainties obtained for V, for both the quartz calibrant and the $NiSO_4 \cdot H_2O$ sample crystal (see Table S3 in the Supporting Information), it is possible to determine accurate values for the parameters of the empirical equations of state (EoS). Therefore, Birch–Murnaghan (BM) equations of state[47] were fitted to V, trying to fit third- and second-order truncations. Evaluating the p–V data (Figure 8a), it is noticeable that despite the two suspected

phase transformations, the evolution of V does not show any discontinuity, thus evidently excluding any of the transitions being first order in character. The fit for the pressure interval relevant for the monoclinic phase (hereinafter referred to as α-$NiSO_4 \cdot H_2O$) revealed a bulk modulus $K_0 = 65.9 \pm 6.7$ GPa and its pressure derivative $K' = 2.3 \pm 4.6$ for a third-order BM-EoS. Considering the error of K_0 and K' as too large, due to the limited number of data points, and K' being too small due to elastic softening effects, K_0 turns to 63.4 ± 1.0 GPa on fitting
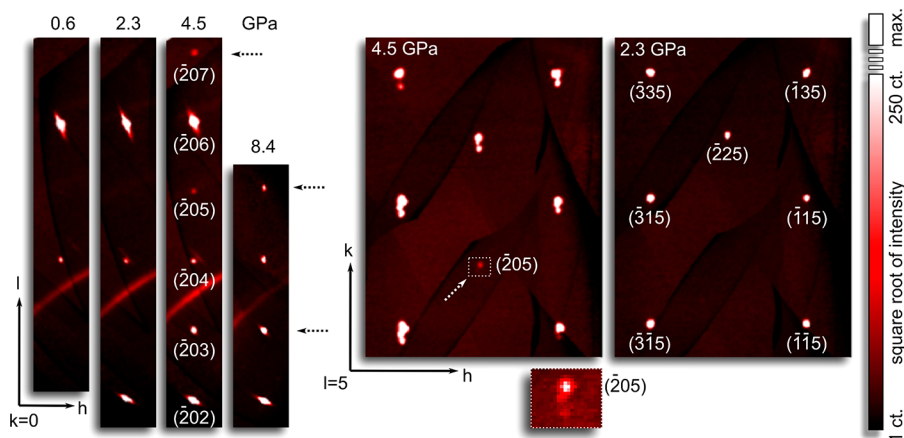
Figure 9. Layers of reconstructed reciprocal space derived from measured frames using the $C2/c$ cell setting. Arrows indicate the appearance of diffraction peaks, which are forbidden in space group $C2/c$. Moreover, the reconstructed $hk5$ layer of the measurement at 4.5 GPa shows split components of individual twin domains following nonmerohedral twinning accompanying the monoclinic-to-triclinic transition.

the data to second-order BM-EoS. Extrapolating the obtained EoS beyond the 2.5 GPa, it can clearly be seen that the V data at higher p deviate between −0.5 Å^3 and +1.3 Å^3 (cf. Figure 8a). The values for the β-NiSO$_4$·H$_2$O polymorph in the range 2.5 to 6.0 GPa correspond to $K_0 = 44.5 \pm 9.4$ GPa and $K' = 8.2 \pm 3.2$, with a relatively high value for K' due to obvious elastic softening effects as reported for the isostructural phases.[27,28] When the p range is restricted between 4.0 and 6.0 GPa, the fit yields a 500% error value for K_0 and K' for BM-3 EoS and $K_0 = 61.3 \pm 1.9$ GPa for BM-2 EoS. The refinement of p−V data in the area of the supposed transition to γ-NiSO$_4$·H$_2$O was also not possible with BM-3 EoS and provides values of $K_0 = 68.4 \pm 2.0$ GPa for BM-2 EoS, which are higher than those obtained for α- and β-NiSO$_4$·H$_2$O. The bulk moduli for the α- and β-forms of NiSO$_4$·H$_2$O are as expected and follow the Anderson−Anderson relationship[48] comparably to the α- and β-forms of MgSO$_4$·H$_2$O and FeSO$_4$·H$_2$O. The same finding as for the evolution of the volume property can be observed for the individual crystallographic axes (Figure 8b−d), in particular for the b- and c-axes, which show similar p dependencies to those of the volume. The a-axis (Figure 8b) shows an increasing compressibility as evidenced by the increasing rate for $\Delta a/\Delta p$, which would be equivalent to a negative M' value, if all data points were fitted according to a BM-3 formalism with an axial modulus $M_0 = 423.4 \pm 5.3$ GPa and $M' = -2.4 \pm 0.8$. The M' value would also be negative if only the data points above 2.5 GPa were used for fitting the EoS of the β-form of NiSO$_4$·H$_2$O ($M_0 = 437 \pm 25$ GPa, $M' = -3.9 \pm 2.9$). This development is remarkable as it is different in comparison to the other phases (cf. Table 1) and might be indicative for the structural instability of the phase at even higher pressures beyond the maximum p within this experimental series.

High-Pressure Crystal Structures. The scXRD intensity data were collected at $p = 0.6(1)$, $2.3(1)$, $4.5(1)$, and $8.4(1)$ GPa in order to extract structural information for all three potential phases. The results of the refinements are given together with details of the data collection in Table 2, and the resulting parameters (fractional coordinates and isotropic displacement parameters) of the structure models are summarized in the Supporting Information (Tables S4). The refinement at 0.6(1) GPa was performed in $C2/c$ U_{iso} constrained only for the two H atoms, at 2.3(1) GPa in

addition, the U_{iso}'s for the three O atoms were constrained. For the refinements in $P\bar{1}$ at 4.5(1) and 8.4(1) GPa, the H positions were constrained to fixed values in addition to the fixed U_{iso}'s. An attempt for a refinement in $P1$ (at 8.4(1) GPa) was performed with positional constraints according to local $\bar{1}$ symmetry for all atoms. This symmetry was stepwise released for each atom, testing for split positions. However, there was no displacement above the three-sigma limit, apart from O2B, which was then accounted into the disordered $P\bar{1}$ structure (Table S4).

Applying the three-dimensional reconstruction of the reciprocal space from a series of collected frames, the data collections corresponding to α-NiSO$_4$·H$_2$O reveal an untwinned single reciprocal lattice of monoclinic symmetry with systematic Bragg peak extinctions corresponding to $C2/c$ symmetry. Above 2.5 GPa, the reciprocal lattice points show a distinct splitting (cf. Figure 9), which is characteristic of a nonmerohedral twinning corresponding to the symmetry reduction from monoclinic to triclinic lattice metrics. Integration of Bragg peak intensities was achieved either for untwinned single-domain samples or, if twinned, at higher angles where peak separation was large enough. In addition, weak diffraction peaks (Figure 9), which were forbidden in $C2/c$, were observed when the samples transformed to triclinic symmetry, confirming the assumed symmetry change. While the changes for the α-to-β transition around 2.5 GPa are obvious and the reflection conditions support the equivalent $C2/c$-to-$P\bar{1}$ transition, such as reported for FeSO$_4$·H$_2$O,[27] there is no apparent evidence from the diffraction pattern for the supposed β-to-γ transition. With respect to hints from the Raman spectra that the S atoms could be located at different crystallographically independent sites, the reciprocal space of the 8.4(1) GPa measurement was deliberately investigated for the existence of superstructure reflections or satellites as would be expected for a commensurately or incommensurately modulated structure, e.g., Ende et al.[49] Despite adequate attention and careful inspection, neither additional Bragg peaks nor satellite reflections could be detected, despite having applied adequate exposure times for recording the diffraction patterns.

Once any kind of superordinate modulation of the structure could be ruled out, all that remains to be considered is a transformation to acentric $P1$ related to a nonisosymmetric

Table 3. Interatomic Distances (Å) of the NiO_6 and SO_4 Units in $NiSO_4 \cdot H_2O$, According to the Crystallographic Data Given in the Supporting Information (Table S4)[a]

pressure/atoms	10^{-4} GPa[b]	0.6 GPa	2.3 GPa	4.5 GPa	8.4 GPa ($P\bar{1}$)	8.4 GPa ($P\bar{1}$) disordered		
Ni1(A)−O1(A)	2.035(2)	2.032(6)	2.027(7)	2.028(5)	2.021(5)		2.021(5)	
Ni1B−O1B				2.018(5)	1.998(5)		1.999(4)	
Ni1(A)−O2(A)	2.032(2)	2.030(3)	2.019(4)	2.013(6)	2.002(6)		2.003(6)	
Ni1B−O2B				1.998(7)	1.984(7)	O2B1	1.936(26)	O2B2	2.017(24)
Ni1(A)−O3	2.115(1)	2.105(2)	2.088(2)	2.065(9)	2.029(9)		2.035(8)	
Ni1B−O3				2.071(9)	2.046(9)		2.042(8)	
S1−O1(A)	1.459(1)	1.465(3)	1.465(3)	1.458(4)	1.453(7)		1.459(7)	
S1−O1B				1.470(7)	1.458(4)		1.461(4)	
S1−O2(A)	1.484(2)	1.467(6)	1.469(8)	1.481(5)	1.476(5)		1.478(5)	
S1−O2B				1.488(13)	1.490(13)	O2B1	1.56(4)	O2B2	1.44(3)

pressure/atoms	10^{-4} GPa[b]	0.6 GPa	2.3 GPa	4.5 GPa	8.4 GPa ($P\bar{1}$)		8.4 GPa ($P\bar{1}$) disordered	
Ni1(A)−O1(A)	2.035(2)	2.032(6)	2.027(7)	2.028(5)	2.021(5)		2.021(5)	
Ni1B−O1B				2.018(5)	1.998(5)		1.999(4)	
Ni1(A)−O2(A)	2.032(2)	2.030(3)	2.019(4)	2.013(6)	2.002(6)		2.003(6)	
Ni1B−O2B				1.998(7)	1.984(7)	O2B1	1.936(26)	O2B2 2.017(24)
Ni1(A)−O3	2.115(1)	2.105(2)	2.088(2)	2.065(9)	2.029(9)		2.035(8)	
Ni1B−O3				2.071(9)	2.046(9)		2.042(8)	
S1−O1(A)	1.459(1)	1.465(3)	1.465(3)	1.458(4)	1.453(7)		1.459(7)	
S1−O1B				1.470(7)	1.458(4)		1.461(4)	
S1−O2(A)	1.484(2)	1.467(6)	1.469(8)	1.481(5)	1.476(5)		1.478(5)	
S1−O2B				1.488(13)	1.490(13)	O2B1	1.56(4)	O2B2 1.44(3)

[a]The O2B positions is split into two positions (O2B1 and O2B2) for the disordered model of the $P\bar{1}$ structure at 8.4 GPa. [b]Data from Giester and Wildner.[15]

Table 4. Bond Angles (deg) in $NiSO_4 \cdot H_2O$ According to the Crystallographic Data Given in the Supporting Information (Table S4)[a]

pressure/atoms	10^{-4} GPa[b]	0.6 GPa	2.3 GPa	4.5 GPa	8.4 GPa ($P\bar{1}$)	8.4 GPa ($P\bar{1}$) disordered	
Ni1(A)−O3−Ni1(B)	123.61(1)	123.5(2)	122.68(1)	121.9(4)	121.0(4)	120.9(3)	
Ni1A−O1A−S1	136.82(9)	136.3(3)	134.6(3)	132.1(3)	130.8(4)	130.4(3)	
Ni1B−O1B−S1				133.0(4)	130.9(4)	130.9(4)	
Ni1A−O2A−S1	130.80(9)	131.0(2)	130.7(2)	125.9(3)	123.0(3)	122.8(3)	
Ni1B−O2B(1/2)−S1				132.6(5)	133.6(5)	131.5(1.8)	134.3(1.7)

[a]Constraints in $P\bar{1}$ (disordered) as stated for Table 3. [b]Data from Giester and Wildner.[15]

Table 5. Interatomic O···O Distances and O2−H Bond Distance (Å) of the Relevant Hydrogen Bonds in $NiSO_4 \cdot H_2O$ According to the Crystallographic Data Given in Supporting Information (Table S4)[a]

pressure/atoms	10^{-4} GPa[b]	0.6 GPa	2.3 GPa	4.5 GPa	8.4 GPa ($P\bar{1}$)	8.4 GPa ($P\bar{1}$) disordered	
O3···O2(A)	2.673(2)	2.674(5)	2.647(6)	2.617(9)	2.592 (9)	2.577(9)	
O3···O2B(1/2)				2.616(7)	2.579(6)	2.529(37)	2.556(18)
O3···O1(A)	3.374(2)	3.357(5)	3.296(5)	3.436(8)	3.470(8)	3.470 (7)	
O3···O1B				3.016(7)	2.852(7)	2.851(6)	
O2(A)−H	1.96(3)	1.71(14)	1.80(13)	1.76(7)	1.757(6)[c]	1.756(6)[c]	
O2B(1/2)−H				1.67(7)	1.901(7)[c]	1.895(25)[c]	1.895(25)[c]

[a]Constraints in $P\bar{1}$ (disordered) as stated for Table 3. [b]Data from Giester and Wildner.[15] [c]Low shown error, due to fixed hydrogen position.

structural change. A refinement of a structural model in $P1$ was achieved by stepwise releasing the symmetry constraints of the inversion center of individual atoms between corresponding atoms in $P\bar{1}$. The refinement of various soft-constrained models finally leads to a significant improvement of the reliability indices (Table 2) only if the O2B was split into two components (O2B1 and O2B2) as done for a proposed $P\bar{1}$ structure with disordered O2B position.

According to the findings from vibrational spectroscopy, the structure is retained without any changes in the bonding topology of the heterodesmic framework, which is composed of octahedral NiO_6 and tetrahedral SO_4 units as described by Giester.[25] The evolution of bond distances is independent of symmetry and does not provide any significant change that could be responsible for the transitions (Tables 3 and 4). This is in complete agreement what has been reported for the $C2/c$-to-$P\bar{1}$ transition from the ambient α- to the high-p β-polymorph of $FeSO_4 \cdot H_2O$.[27] In accordance with the displacive changes observed in this isostructural compound, a tendency of the framework to fold up can be anticipated for $NiSO_4 \cdot H_2O$ as well, as could be observed on the bond angles on the bridging oxygen atoms. There is a general decrease of Ni−O−Ni and Ni−O−S angles as a consequence of the compacting

folding, together with the diversification of Ni−O2−S angles (126° vs 133° at 4.5 GPa) in the same manner as reported for $FeSO_4 \cdot H_2O$ upon exceeding the α-to-β transition point. Looking more closely at the development at the second critical point around 6.5 GPa, it can be seen that two resulting sulfate tetrahedra actually reveal different bond-length distortions with respect to their individual S−O bond lengths (e.g., S1−O2B1 = 1.56(4) Å, S1−O2B2 = 1.44(3) Å at 8.4(1) GPa). However, the true crystallographic symmetry of the main framework is yet not beyond doubt $P\bar{1}$. The shown model has to be assumed to be an approximated model. One can prove beyond doubt the development of crystallographically different sites, which is just most pronounced in the case of the O2B positions. Within the obtained uncertainties from the structure refinement, the symmetry lowering recognizable from the Raman spectra beyond 7 GPa can be confirmed.

Hydrogen Bonding under Pressure. While the transformations do not cause virtually any changes with respect to the main structural units of the framework, with the exception of some polyhedral tilting leading to higher compaction, the hydrogen bonding system reveals notable changes at the critical transition points. Due to the loss of the local 2-fold axis
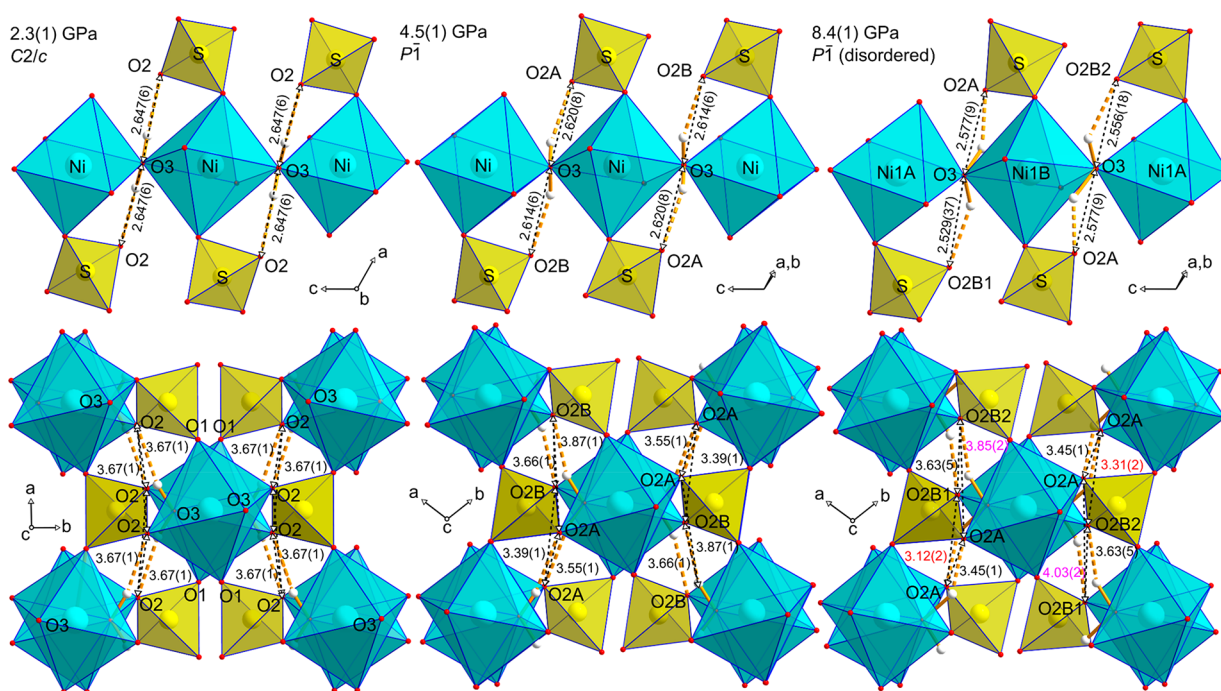
Figure 10. Hydrogen-bonding system and polyhedral connections in the α, β, and γ forms of $NiSO_4 \cdot H_2O$ at 2.3(1), 4.5(1), and 8.4(1) GPa. For each form, two directions are shown, one perpendicular (upper part) and the other parallel (lower part) to the octahedral-chain units. In the triclinic forms, the voids around the hydrogen atoms form series along the a and b axes, which show different pressure-dependent compression behavior starting around 2.5 GPa. Therefore, different void sizes (as determined by the O2···O2 distances) can be recognized with respect to the hydrogen bonds parallel to the different axes.

associated with the $C2/c$-to-$P\bar{1}$ transition, the symmetry equivalent pair of O3···O2 hydrogen bonds (O3···O2 distance: 2.647(6) Å at 2.3(1) GPa) as well as a further pair of intermolecular O3···O1 distances (3.296(5) Å at 2.3(1) GPa) become distinguishable as four symmetry-independent distances (Table 5). As in $MgSO_4 \cdot H_2O$[28] and $FeSO_4 \cdot H_2O$,[27] the lattice distortion causes one of the O3···O1 distances to be drastically shortened (from 3.296(5) Å at 2.3(1) GPa to 2.851(6) Å at 8.4(1) GPa) thus becoming potentially involved in the hydrogen-bonding system (Figure 10). These changes confirm the mechanism reported for the α-to-β transition in the analogous ferrous compound with the development of three short O3···O contacts suitable as relevant hydrogen bonds with O3 being the donator oxygen. As found in the isostructural compounds, the O3···O1 contacts show a significant diversification with respect to their interatomic distances, i.e., the significant shortening of O3···O1B from 3.296(5) Å (at 2.3(1) GPa) to 3.016(7) Å (at 4.5(1) GPa) while the O3···O1A distance even increases in length (to 3.436(8) Å at 4.5(1) GPa) upon crossing the critical transition point around 2.5 GPa. As the voids, in which the hydrogen atoms are positioned, are oriented along the a and b axes, their different pressure-dependent compression behavior starting around 2.5 GPa is manifested in noticeably different void sizes (O2···O2 distances) visible in Figure 10.

Of particular interest are the changes in the hydrogen-bonding system when the second transformation point is exceeded around 6.5 GPa. There, the relevant O···O distances are subject to only minor changes, and the bond-length differences are only relatively small (e.g., O3···O2 = 2.53(4) and 2.56(2) Å). It is therefore obvious that the second structural change is not primarily due to the hydrogen-bonding system and apparently only adapts to the small changes arising

from the framework as discussed above. However, similar to the first transition, the second one is mostly affecting the size of the voids hosting the hydrogen atoms (Figure 10). It even affects them in the same fashion by further increasing the long O2···O2 distances (which are oriented along the a axis), while the short O2···O2 distances (which are oriented along the b-axis direction) decrease (O2A···O2B2: 3.306(24) Å vs O2A···O2B1: 3.115(24) Å and O2B1···O2A: 4.032(23) Å vs O2B2···O2A: 3.859(22) Å, Figure 10).

■ CONCLUSIONS

The in situ high-p investigations on nickel sulfate monohydrate reveal two apparent structural instabilities accompanied by transformations under isothermal hydrostatic compression. While the first transition observed in $NiSO_4 \cdot H_2O$ occurs at 2.47(1) GPa, showing all features equivalent to the ferroelastic transformations reported in isostructural $MgSO_4 \cdot H_2O$ (p_c = 2.72 GPa) and $FeSO_4 \cdot H_2O$ (p_c = 6.15 GPa), this study reveals a second subtle structural change in $NiSO_4 \cdot H_2O$ at 6.5(5) GPa. The ferroelastic $C2/c$-to-$P\bar{1}$ transition at 2.47 GPa is identical in its character to those described so far for the isostructural compounds. In particular, the type of lattice changes as described by the settings in $C2/c$ and its reduced cell are more or less identical, such as the interatomic distances of the O···O contacts within the hydrogen-bonding system, which change in the same fashion. Comparing the high-p behavior of the three known kieserite-type representatives and their critical transition pressures p_c (2.47, 2.72, 6.15 GPa), the unit-cell volumes (342.3, 355.5, 365.2 Å^3), and the bulk moduli K_0 (63.4, 48.1 45.2 GPa) with respect to the ionic radii[50] of the particular M^{2+} cations (0.69, 0.72, 0.78 Å), $NiSO_4 \cdot H_2O$ reveals the lowest p_c and the highest value for K_0. This could be expected since it is the compound with the smallest M^{2+} cation

and thus the smallest unit-cell volume of the α-phase. Although the bulk modulus is affected by the large uncertainty and might be overestimated due to the fact that the available pressure interval is the shortest among all representatives, it follows more or less the Anderson−Anderson relationship[48] (i.e., $V_0 \times K_0 \approx$ constant) with 21 702, 17 099, and 16 507 Å$^3\cdot$GPa for the Ni, Mg, and Fe end members, respectively.

When comparing the compressibilities along the different lattice directions, it is striking that the a-axis shows a noticeable negative compressibility ($M' = -3.9 \pm 2.9$, BM-3 all data points above 2.5 GPa) for the β-phase of NiSO$_4\cdot$H$_2$O, which has not been observed for the other two compounds. Negative values for the pressure derivatives of axial moduli have been found in many cases to indicate a structural instability, which in turn might act as the precursor of the β-to-γ transition around 6.5 GPa. In this respect, it is not surprising that a further transformation was indeed observed. The second transition is evident from results of independent analytical techniques, on the one hand by the splitting of the Raman band attributed to the $\nu_1(SO_4)$ mode and on the other hand by observing higher values for the reliability indices for the structure refinement of data sets measured beyond 6.5 GPa. Although weak satellite reflections could not be observed within the data sets of this study, the true symmetry of the γ-phase and the existence of a superstructure cannot be completely ruled out, especially if it is based only on slight changes in the oxygen and hydrogen positions. Therefore, the relevant Bragg peak intensities are possibly far below the detectable signal-to-noise ratio in our DAC measurement. Nevertheless, the presented model of the structure at 8.4(1) GPa reveals pseudocentrosymmetry of the heavy atoms when refining in $P1$ global symmetry, where the symmetry coupling of centrosymmetric positions was released stepwise for each pair of atoms. Only the oxygen atoms indicated deviations from centrosymmetry with the effect being most significant for the O2 positions. The differences between a proper refinement in $P\bar{1}$ and with local symmetry constraints in $P1$ are evident (Table 2) and provide an additional proof for the existence of a third polymorph. The transition pathway is determined by the symmetry relationship with monoclinic $C2/c$ (α-NiSO$_4\cdot$H$_2$O) and triclinic $P\bar{1}$ (β-NiSO$_4\cdot$H$_2$O) and a disordered O2B position in $P\bar{1}$ (γ-NiSO$_4\cdot$H$_2$O).

Polymorphism of M^{2+}SO$_4\cdot$H$_2$O is an important topic in astrophysics and planetary geology with respect to the monohydrate sulfates being an abundant component on the surface of icy moons (cf. Comodi et al.[51] and McCord et al.[52]). α-MgSO$_4\cdot$H$_2$O and β-MgSO$_4\cdot$H$_2$O have recently been considered for the interior of Callisto,[28] where the maximum pressure corresponds to around 5 GPa. Considering the significant Ni contents in the soluble sulfate fraction in C1/C2 carbonaceous chondrites believed to be chemically similar to the rocky cores of the icy moons (e.g., Ivuna and Orgueil) and meteorites with up to 13.6 wt % NiO,[13] NiSO$_4\cdot$H$_2$O can be considered as an important component in natural mono-hydrate sulfates. According to previously reported findings, there is a tendency of the enrichment of Ni relative to Mg during the crystallization of solid nickel−magnesium sulfate from aqueous Mg−Ni-containing solutions.[5] As the first critical transition in NiSO$_4\cdot$H$_2$O occurs at even lower pressure than in kieserite itself, the occurrence of the high-p β-form is therefore very likely wherever Ni substitution occurs.

■ ASSOCIATED CONTENT

ⓢ Supporting Information

The Supporting Information is available free of charge at https://pubs.acs.org/doi/10.1021/acs.inorgchem.0c00370.

Refined triclinic and monoclinic lattice parameters and unit-cell volumes; fractional atomic coordinates of the α, β, and γ-crystal structures as well as isotropic displacement parameters; photograph of a NiSO$_4\cdot$H$_2$O sample crystal inside the pressure chamber compressed in a dense methanol/ethanol mixture at 10.8 GPa; dendrogram of a hierarchical cluster analysis and subsequent principle cluster analysis of pressure induced Raman shifts (PDF)

Accession Codes

CCDC 1981955−1981958 contain the supplementary crystallographic data for this paper. These data can be obtained free of charge via www.ccdc.cam.ac.uk/data_request/cif, or by emailing data_request@ccdc.cam.ac.uk, or by contacting The Cambridge Crystallographic Data Centre, 12 Union Road, Cambridge CB2 1EZ, UK; fax: +44 1223 336033.

■ AUTHOR INFORMATION

Corresponding Author

Martin Ende − *Department of Mineralogy and Crystallography, University of Vienna, A-1090 Wien, Austria;* ⓞ orcid.org/0000-0002-9509-8543; Email: martin.ende@univie.ac.at

Authors

Terhi Kirkkala − *Department of Chemistry, University of Jyväskylä, FI-40014 Jyväskylä, Finland*
Michael Loitzenbauer − *Department of Mineralogy and Crystallography, University of Vienna, A-1090 Wien, Austria*
Dominik Talla − *Department of Mineralogy and Crystallography, University of Vienna, A-1090 Wien, Austria*
Manfred Wildner − *Department of Mineralogy and Crystallography, University of Vienna, A-1090 Wien, Austria*
Ronald Miletich − *Department of Mineralogy and Crystallography, University of Vienna, A-1090 Wien, Austria*

Complete contact information is available at:
https://pubs.acs.org/10.1021/acs.inorgchem.0c00370

Notes

The authors declare no competing financial interest.

■ REFERENCES

(1) Bibring, J.-P.; Langevin, Y.; Mustard, J. F.; Poulet, F.; Arvidson, R.; Gendrin, A.; Gondet, B.; Mangold, N.; Pinet, P.; Forget, F.; Berthe, M.; Bibring, J.-P.; Gendrin, A.; Gomez, C.; Gondet, B.; Jouglet, D.; Poulet, F.; Soufflot, A.; Vincendon, M.; Combes, M.; Drossart, P.; Encrenaz, T.; Fouchet, T.; Merchiorri, R.; Belluci, G.;

Altieri, F.; Formisano, V.; Capaccioni, F.; Cerroni, P.; Coradini, A.; Fonti, S.; Korablev, O.; Kottsov, V.; Ignatiev, N.; Moroz, V.; Titov, D.; Zasova, L.; Loiseau, D.; Mangold, N.; Pinet, P.; Doute, S.; Schmitt, B.; Sotin, C.; Hauber, E.; Hoffmann, H.; Jaumann, R.; Keller, U.; Arvidson, R.; Mustard, J. F.; Duxbury, T.; Forget, F.; Neukum, G. Global Mineralogical and Aqueous Mars History Derived from OMEGA/Mars Express Data. *Science* **2006**, *312*, 400–404.

(2) Gendrin, A.; Mangold, N.; Bibring, J. P.; Langevin, Y.; Gondet, B.; Poulet, F.; Bonello, G.; Quantin, C.; Mustard, J.; Arvidson, R.; LeMouélic, S. Sulfates in Martian Layered Terrains: The OMEGA/Mars Express View. *Science* **2005**, *307*, 1587.

(3) Langevin, Y.; Poulet, F.; Bibring, J. P.; Gondet, B. Sulfates in the North Polar Region of Mars Detected by OMEGA/Mars Express. *Science* **2005**, *307*, 1584.

(4) Murchie, S. L.; Mustard, J. F.; Ehlmann, B. L.; Milliken, R. E.; Bishop, J. L.; McKeown, N. K.; Noe Dobrea, E. Z.; Seelos, F. P.; Buczkowski, D. L.; Wiseman, S. M.; Arvidson, R. E.; Wray, J. J.; Swayze, G.; Clark, R. N.; Des Marais, D. J.; McEwen, A. S.; Bibring, J.-P. A synthesis of Martian aqueous mineralogy after 1 Mars year of observations from the Mars Reconnaissance Orbiter. *J. Geophys. Res.* **2009**, *114*, No. E00D06.

(5) Kargel, J. S. Brine volcanism and the interior structures of asteroids and icy satellites. *Icarus* **1991**, *94*, 368–390.

(6) McCord, T. B.; Hansen, G. B.; Matson, D. L.; Johnson, T. V.; Crowley, J. K.; Fanale, F. P.; Carlson, R. W.; Smythe, W. D.; Martin, P. D.; Hibbitts, C. A.; Granahan, J. C.; Ocampo, A. Hydrated salt minerals on Europa's surface from the Galileo near-infrared mapping spectrometer (NIMS) investigation. *J. Geophys. Res.* **1999**, *104*, 11827–11851.

(7) Gromnitskaya, E. L.; Yagafarov, O. F.; Lyapin, A. G.; Brazhkin, V. V.; Wood, I. G.; Tucker, M. G.; Fortes, A. D. The high-pressure phase diagram of synthetic epsomite ($MgSO_4 \cdot 7H_2O$ and $MgSO_4 \cdot 7D_2O$) from ultrasonic and neutron powder diffraction measurements. *Phys. Chem. Miner.* **2013**, *40*, 271–285.

(8) Wang, W.; Fortes, A. D.; Dobson, D. P.; Howard, C. M.; Bowles, J.; Hughes, N. J.; Wood, I. G. Investigation of high-pressure planetary ices by cryo-recovery. II. High-pressure apparatus, examples and a new high-pressure phase of $MgSO_4 \cdot 5H_2O$. *J. Appl. Crystallogr.* **2018**, *51*, 692–705.

(9) Fortes, A. D.; Knight, K. S.; Wood, I. G. Structure, thermal expansion and incompressibility of $MgSO_4 \cdot 9H_2O$, its relationship to meridianiite ($MgSO_4 \cdot 11H_2O$) and possible natural occurrences. *Acta Crystallogr., Sect. B: Struct. Sci., Cryst. Eng. Mater.* **2017**, *73*, 47–64.

(10) Fortes, A. D.; Fernandez-Alonso, F.; Tucker, M. G.; Wood, I. G. Isothermal equation of state and high-pressure phase transitions of synthetic meridianiite ($MgSO_4 \cdot 11D_2O$) determined by neutron powder diffraction and quasielastic neutron spectroscopy. *Acta Crystallogr., Sect. B: Struct. Sci., Cryst. Eng. Mater.* **2017**, *73*, 33–46.

(11) Fortes, A. D.; Wood, I. G.; Alfredsson, M.; Vocadlo, L.; Knight, K. S. The thermoelastic properties of $MgSO_4 \cdot 7D_2O$ (epsomite) from powder neutron diffraction and ab initio calculation. *Eur. J. Mineral.* **2006**, *18*, 449–462.

(12) Wang, A.; Freeman, J. J.; Jolliff, B. L. Phase transition pathways of the hydrates of magnesium sulfate in the temperature range 50°C to 5°C: Implication for sulfates on Mars. *J. Geophys. Res.* **2009**, *114*, No. E04010.

(13) Fredriksson, K.; Kerridge, J. F. Carbonates and Sulfates in Chondrites: Formation by Aqueous Activity on the Parent Body. *Meteoritics* **1988**, *23*, 35–44.

(14) Fortes, A. D.; Knight, K. S.; Gibbs, A. S.; Wood, I. G. Crystal structures of $NiSO_4 \cdot 9H_2O$ and $NiSO_4 \cdot 8H_2O$: magnetic properties, stability with respect to morenosite ($NiSO_4 \cdot 7H_2O$), the solid-solution series (Mg_xNi_{1-x})$SO_4 \cdot 9H_2O$. *Phys. Chem. Miner.* **2018**, *45*, 695–712.

(15) Wildner, M.; Giester, G. The crystal structures of kieserite-type compounds. I. Crystal structures of Me(II)$SO_4 \cdot H_2O$ [Me = Mn, Fe, Co, Ni, Zn]. *Neues Jb. Miner. Monat.* **1981**, *7*, 296–306.

(16) Giester, G.; Lengauer, C. L.; Redhammer, G. J. Characterization of the $FeSO_4 \cdot H_2O$-$CuSO_4 \cdot H_2O$ solid-solution series, and the nature of poitevinite, (Cu,Fe)$SO_4 \cdot H_2O$. *Can. Mineral.* **1994**, *32*, 873–884.

(17) Bechtold, A.; Wildner, M. Crystal chemistry of the kieserite-cobaltkieserite solid solution, $Mg_{1-x}Co_x(SO_4) \cdot H_2O$: well behaved oddities. *Eur. J. Mineral.* **2016**, *28*, 43–52.

(18) Elgersma, F.; Witkamp, G. J.; van Rosmalen, G. M. Incorporation of zinc in ferrous sulfate monohydrate. *Hydrometallurgy* **1993**, *33*, 301–311.

(19) Stoilova, D.; Lutz, H. D. Infrared study of ν_{OD} modes in isotopically dilute (HDO) kieserite-type compounds $MXO_4 \cdot H_2O$ (M = Mn, Co, Ni, Zn, and X = S, Se) with matrix-isolated M'^{2+} and $X'O_4^{2-}$ guest ions. *J. Mol. Struct.* **1998**, *450*, 101–106.

(20) Giester, G.; Wildner, M. The crystal structures of kieserite -type compounds. II. Crystal structures of Me(II)$SeO_4 \cdot H_2O$ (Me = Mg, Mn, Co, Ni, Zn). *Neues Jb. Miner. Monat.* **1992**, *3*, 135–144.

(21) Boonchom, B.; Youngme, S.; Maensiri, S.; Danvirutai, C. Nanocrystalline serrabrancaite ($MnPO_4 \cdot H_2O$) prepared by a simple precipitation route at low temperature. *J. Alloys Compd.* **2008**, *454*, 78–82.

(22) Witzke, T.; Wegner, R.; Doering, T.; Pöllmann, H.; Schuckmann, W. Serrabrancaite, $MnPO_4 \cdot H_2O$, a new mineral from the Alto Serra Branca pegmatite, Pedra Lavrada, Paraiba, Brazil. *Am. Mineral.* **2000**, *85*, 847–849.

(23) Leonhardt, J.; Weiss, R. Das Kristallgitter des Kieserits $MgSO_4 \cdot H_2O$. *Naturwissenschaften* **1957**, *44*, 338–339.

(24) Hawthorne, F. C.; Groat, L. A.; Raudsepp, M.; Ercit, T. S. Kieserite, $Mg(SO_4)(H_2O)$, A titanite-group mineral. *Neues Jb Miner. Abh.* **1987**, *157*, 121–132.

(25) Giester, G. The crystal structures of $CuSO_4 \cdot H_2O$ and $CuSeO_4 \cdot H_2O$, and their relationships to kieserite. *Mineral. Petrol.* **1988**, *38*, 277–283.

(26) Bregeault, J. M.; Herpin, P. Crystal structure of $CdSO_4 \cdot H_2O$. *Bull. Soc. Franc. Minéral. Cristallogr.* **1970**, *93*, 37–42.

(27) Meusburger, J. M.; Ende, M.; Talla, D.; Wildner, M.; Miletich, R. Transformation mechanism of the pressure-induced C2/c-to-P transition in ferrous sulfate monohydrate single crystals. *J. Solid State Chem.* **2019**, *277*, 240–252.

(28) Meusburger, J. M.; Ende, M.; Matzinger, P.; Talla, D.; Miletich, R.; Wildner, M. Polymorphism of Mg-monohydrate sulfate kieserite under pressure and its occurrence on giant icy Jovian satellites. *Icarus* **2020**, *336*, 113459.

(29) Talla, D.; Wildner, M. Investigation of the kieserite–szomolnokite solid-solution series, (Mg,Fe)$SO_4 \cdot H_2O$, with relevance to Mars: Crystal chemistry, FTIR, and Raman spectroscopy under ambient and martian temperature conditions. *Am. Mineral.* **2019**, *104*, 1732–1749.

(30) Miletich, R.; Allan, D. R.; Kuhs, W. F. High-Pressure Single-Crystal Techniques. *Rev. Mineral. Geochem.* **2000**, *41*, 445–519.

(31) Boehler, R.; De Hantsetters, K. New anvil designs in diamond cells. *High Pressure Res.* **2004**, *24*, 391–396.

(32) Scheidl, K. S.; Kurnosov, A.; Trots, D. M.; Boffa Ballaran, T.; Angel, R. J.; Miletich, R. Extending the single-crystal quartz pressure gauge up to hydrostatic pressure of 19 GPa. *J. Appl. Crystallogr.* **2016**, *49*, 2129–2137.

(33) Jacobsen, S. D.; Holl, C. M.; Adams, K. A.; Fischer, R. A.; Martin, E. S.; Bina, C. R.; Lin, J.-F.; Prakapenka, V. B.; Kubo, A.; Dera, P. Compression of single-crystal magnesium oxide to 118 GPa and a ruby pressure gauge for helium pressure media. *Am. Mineral.* **2008**, *93*, 1823–1828.

(34) Mao, H. K.; Xu, J.; Bell, P. M. Calibration of the ruby pressure gauge to 800 kbar under quasi-hydrostatic conditions. *J. Geophys. Res.* **1986**, *91*, 4673–4676.

(35) Chijioke, A. D.; Nellis, W. J.; Soldatov, A.; Silvera, I. F. The ruby pressure standard to 150 GPa. *J. Appl. Phys.* **2005**, *98*, 114905.

(36) Angel, R. J.; Finger, L. W. SINGLE: a program to control single-crystal diffractometers. *J. Appl. Crystallogr.* **2011**, *44*, 247–251.

(37) King, H. E.; Finger, L. W. Diffracted beam crystal centring and its application to high-pressure crystallography. *J. Appl. Crystallogr.* **1979**, *12*, 374–378.

(38) Gonzalez-Platas, J.; Alvaro, M.; Nestola, F.; Angel, R. EosFit7-Gui: A new graphical user interface for equation of state calculations, analyses and teaching. *J. Appl. Crystallogr.* **2016**, *49*, 1377−1382.

(39) Angel, R.; Gonzalez-Platas, J. Absorb-7 and Absorb-GUI for single-crystal absorption corrections. *J. Appl. Crystallogr.* **2013**, *46*, 252−254.

(40) Prince, E. *International Tables for Crystallography*, third ed.; Kluwer Academic Publishers, 2004; Vol. C, p 1000.

(41) Sheldrick, G. M. Crystal structure refinement with SHELXL. *Acta Crystallogr., Sect. C: Struct. Chem.* **2015**, *71*, 3−8.

(42) Hübschle, C. B.; Sheldrick, G. M.; Dittrich, B. ShelXle: A Qt graphical user interface for SHELXL. *J. Appl. Crystallogr.* **2011**, *44*, 1281−1284.

(43) Chio, C. H.; Sharma, S. K.; Muenow, D. W. The hydrates and deuterates of ferrous sulphates($FeSO_4$): a Raman spectroscopic study. *J. Raman Spectrosc.* **2007**, *38*, 87−99.

(44) Talla, D., Balla, M., Aicher, C., Lengauer, C. L., Lengauer, L., Wildner, M. Structural and spectroscopic study of the kieserite-dwornikite solid solution series, $(Mg,Ni)SO_4·H_2O$, at ambient and lowtemperatures, with cosmochemical implications for icy moons and Mars. *Am. Mineral.* **2020**, DOI: 10.2138/am-2020-7287.

(45) Ende, M.; Wunder, B.; Koch-Müller, M.; Pippinger, T.; Buth, G.; Giester, G.; Lengauer, C. L.; Libowitzky, E. T-induced displacive phase transition of Pb-lawsonite end member. *Mineral. Mag.* **2016**, *80*, 249−267.

(46) Carpenter, M. A.; Salje, E. K. H.; Graeme-Barber, A. Spontaneous strain as a determinant of thermodynamic properties for phase transitions in minerals. *Eur. J. Mineral.* **1998**, *10*, 621−691.

(47) Birch, F. Finite Elastic Strain of Cubic Crystals. *Phys. Rev.* **1947**, *71*, 809−824.

(48) Anderson, D. L.; Anderson, O. L. The bulk modulus-volume relationship for oxides. *J. Geophys. Res.* **1970**, *75*, 3494−3500.

(49) Ende, M.; Effenberger, H.; Miletich, R. Evolution of the α-$BaMg(CO_3)_2$ low-temperature superstructure and the tricritical nature of its $\alpha−\beta$ phase transition. *Acta Crystallogr., Sect. B: Struct. Sci., Cryst. Eng. Mater.* **2017**, *73*, 827−835.

(50) Shannon, R. D. Revised Effective Ionic Radii and Systematic Study of Inter Atomic Distances in Halides and Chalcogenides. *Acta Crystallogr., Sect. A: Cryst. Phys., Diffr., Theor. Gen. Crystallogr.* **1976**, *32*, 751−767.

(51) Comodi, P.; Stagno, V.; Zucchini, A.; Fei, Y.; Prakapenka, V. The compression behaviour of blödite at low and high temperature up to ~ 10 GPa: Implications for the stability of hydrous sulfates on icy planetary bodies. *Icarus* **2017**, *285*, 137−144.

(52) McCord, T. B.; Hansen, G. B.; Hibbits, C. A. Hydrated salt minerals on Ganymede's surface: evidence of an ocean below. *Science* **2001**, *292*, 1523−1525.